An appraisal of large-scale particle tracking with uncrewed aerial vehicles

R. Leister[1,2,*], D.E. Rival[2,3]

1: Institute of Fluids Mechanics (ISTM), Karlsruhe Institute of Technology, Germany
2: Department of Mechanical and Materials Engineering, Queen's University, Kingston, Canada
3: Institute Institute of Fluid Mechanics, Technische Universität Braunschweig, Germany
*Corresponding author: robin.leister@kit.edu

Keywords: Particle Tracking, large-scale PTV, drone PTV, uncrewed aerial vehicle

ABSTRACT

Camera technology is rapidly enhancing within the last years, which led to the availability of sophisticated technical features within consumer cameras, that could only be found in scientific set-ups earlier. The present work explores the possibilities of utilizing the potentials of commercially-available camera drones as moving cameras for large-scale particle tracking velocimetry. We made use of the glare-point particle tracking approach introduced by Kaiser & Rival (2023), where only a single camera and natural illumination, e.g. the sun, could be used. The set-up demonstrated full suitability for large volumes in the order of 10-100 m^3. The frame-to-frame camera movement, caused by the slight movement of the drone could be quantified and corrected by an imaged-based approach. The calibration strategy could be simplified due to the fixed set-up in the camera drone. The limits introduced through the tracer size and uncertainty caused by the glare-point approach are discussed accordingly. For the presented magnification and camera set-up given by the *DJI Mini 3 pro*, the limit in height can be determined when the two most dominant glare points collapse to one, which happened well above 10 m for the present set-up. The equipment together with the glare-point particle tracking approach is best suited for flow information extraction at large-scale facilities or difficult accessible terrain, where the current set-up could depict its strengths.

1. Introduction

Current development in camera technology during the latest years lead to the availability of drones with cameras, that include a considerable large amount of technical features, that could only be found in a high-end camera several years ago. Major steps in current advances are the availability of higher frame rates, the recorded video depth of more than 8 bit per channel and a considerably high image resolution with the current trend of 4k video. However, for a scientific set-up these cameras lack some important features, like a global image shutter or a precise trigger, among

others. Over the last years, several companies have introduced commercial grade camera drones, with a remarkable improvement of imaging and stabilization technique.

Aerial vehicles were already used since the first image-based velocimetry approaches found its way into fluid-mechanic research. Such as Fujita & Hino (2003) or Detert & Weitbrecht (2014), where helicopters were used, equipped with a camera to extract velocity information of flowing river water in a non-intrusive way. As tracers mostly wooden or foam chips were used. The use of off-the-shelf rotary-wing drones, i.e. unmanned or uncrewed aerial vehicles, instead of helicopters for a 2D-PIV evaluation were done by e.g. Detert & Weitbrecht (2015) and Detert et al. (2019). They made use of a 1.6×1.6 m^2 interrogation area with seeding particles in the range of $30 - 40$ mm for the extraction of the surface velocity in a river close to a hydro-power plant.

For an image-based measurement of air movement larger particles with an acceptable following behavior are more difficult to achieve. Rosi et al. (2014) used fog-filled soap bubbles and Wei et al. (2021) used snow as tracers. Hou et al. (2021) and Kaiser & Rival (2023) suggested an approach for large-scale volumetric particle tracking, which made use of the sun as illumination source and of air-filled soap bubbles (AFSB) as tracer particles together with the use of only one camera for 3D3C reconstruction. These facts overcome at least some of the downsides of nowadays-available camera drones for a scientific usage.

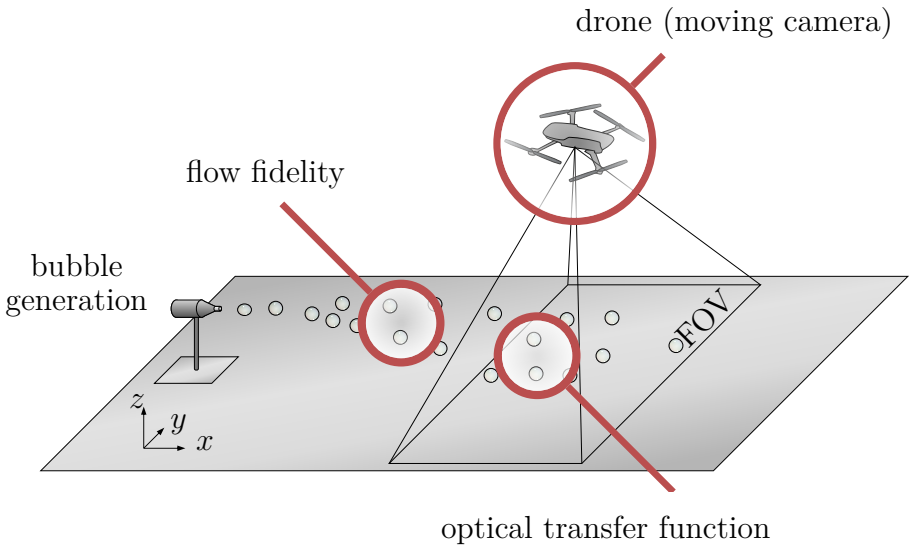

Figure 1. Sketch of the experimental set-up with highlighted problems, that are addressed.

The current investigation therefore aims at an appraisal of camera drones for large-scale particle tracking, as a feasibility study with regard to a scientific evaluation scheme. Such an undertaking is separated into different scientific problems, such as (i) the problem of air bubble generation with a narrow diameter distribution – which is a requirement for the glare-point approach – (ii) the optical transfer function at different reproduction scales, (iii) the fact that the camera is moving and needs

a continuous calibration and (iv) the overall flow information extracted with this technique. Figure 1 sketches the principle overview and names the addressed problems. The AFSBs are produced via a bubble-generator prototype, which aims at producing bubbles with an equally-distributed diameter.

2. Bubble Generation and Flow Fidelity

Velocimetry measurements by means of optical techniques are in need of the addition of particles, with an opaque surface or a different refractive index than the surrounding fluid in order to form a particle image, which can be captured by the imaging device or camera. To make the flow structures visible these particles need to scatter and/or reflect light.

While aersosol-based droplets, e.g. di-ethyl-hexyl-sebacate (DEHS) or water-glycol particles, with a typical diameter in the range of $0.3 - 0.4$ µm (Fuchs et al., 2023), are suitable for small scale measurements and often applied due to their superior following behavior, larger particles with adequate particle-image intensities needs to be employed for measurements at larger scales. Here, especially helium-filled soap bubbles are used as tracer particles in air, since neutral buoyancy can be adjusted. Assuming a gravitationally induced velocity U_g from Stokes drag law, this yields (following Raffel et al., 2018):

$$U_\mathrm{g} = {d_\mathrm{p}}^2 \frac{(\rho_\mathrm{p} - \rho)}{18\mu} g, \tag{1}$$

where d_p is the particle diameter, ρ and ρ_p the fluid and particle density, respectively, and μ the dynamic viscosity of the fluid. Figure 2 shows the visualization of Eq. (1) for different particle sizes and density values, which result from different bubble-wall thicknesses γ. Acceleration caused by the gravitation or other forces are therefore depicted properly for smaller particle diameters or thin bubble-wall thicknesses γ. For low values of γ the slip velocity is comparatively small even for relatively large bubble diameters. A well-chosen particle generation system, where the bubble diameter and the amount of used soap fluid can be adjusted individually it therefore decisive for a meaningful fluid flow analysis with such large bubbles as tracer particles.

The rationale behind a well-chosen particle generation is two-fold. The glare-point approach introduced by Hou et al. (2021) makes use of the glare-point distance to extract the third spatial coordinate and third velocity component. Hence, a precise knowledge of the bubbles diameter – ideally of each individual bubble – is decisive. Hou et al. (2021) and Kaiser & Rival (2023) made use of a second camera for a quantification of the bubble diameter which consequently enables an error estimation during the experiment. The present contribution tries to answer the question of bubble diameter distribution beforehand, to avoid a second camera set-up during the experiment.

Thus a small double-illumination set-up, which combines a backward-illumination to account for the outer edge of the bubble and a forward illumination, for glare-point visibility was built to

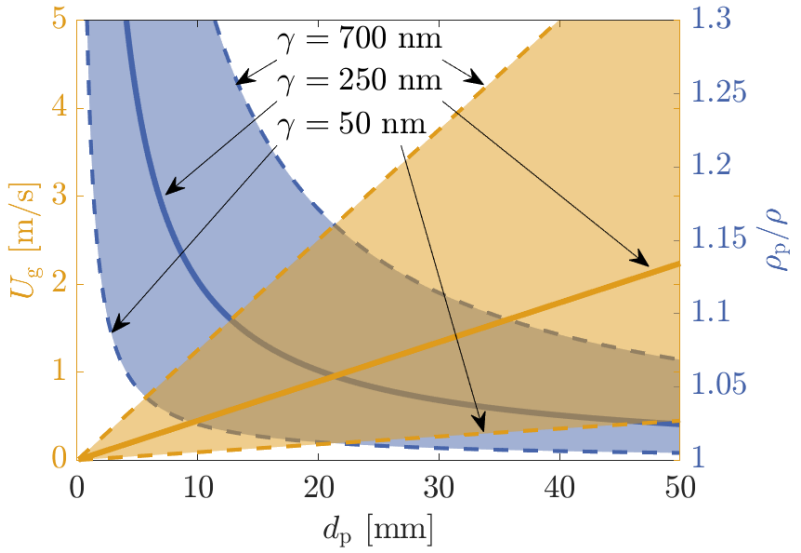

Figure 2. Density ratio (ρ_p/ρ) and slip velocity (U_g) as a function of the bubble diameter d_p. U_g is calculated assuming stokes drag law with Eq. (1). Values are visualized for a range of bubble-wall thicknesses for $\gamma = 50$ nm to 700 nm. The density ratio decreases for larger particle sizes, the slip velocity, however, increases linearly.

quantify the relationship between the change of glare-point-distances, shortly after generation as reported by Kaiser & Rival (2023), and the spherical shape, detected by the outer edge of the bubble in x and y-direction.

Figure 3a shows the glare-point distance as well as the outer shapes for one bubble closely after generation. All considered values fluctuate in time, due to the bubble deformation in the first time span after leaving the bubble generator. However, as most sensitive parameter the glare-point distance can be identified. While the x and y value oscillate partly in an asynchronous manner, but reduce in magnitude at around 200 ms, the oscillation of the glare-point distance is still pronounced even at 300 ms, when the bubble left the FOV. This fact is convenient for the glare-point tracking approach, since a deviation from the ideal spherical shape of the tracer is indicated distinguishable by the change of glare-point distance in time. The tracer itself calls attention for an imperfect following behavior by a quantity that is visible not only during the laboratory environment, but also during the outdoor experiments. Regions or time instances, where the glare-point distances fluctuate can be considered with particular cautiousness, when the aim is a precise extraction of the underlying fluid flow.

For the generation of equally-sized bubbles a 3D-printed bubble generator was manufactured similar to Kaiser & Rival (2023). Figure 3c shows the corresponding diameter distribution of the generated soap bubbles for one operational point.

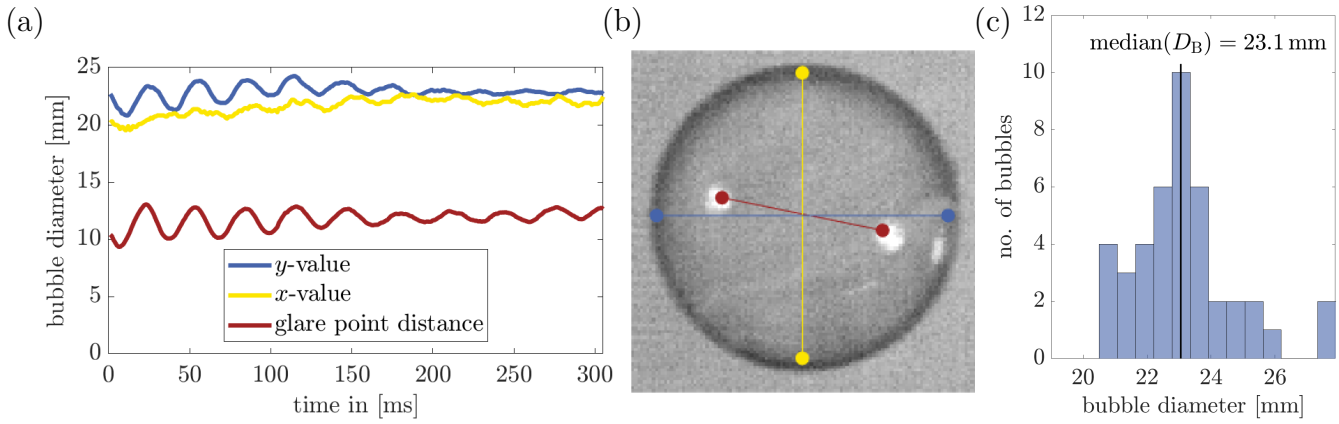

Figure 3. (a) Horizontal, vertical and glare point distance over time over one bubble. (b) Raw data of one bubble with indication of the horizontal edge (• $y-$values), the vertical edge (• x-values) and the glare point distance (•). (c) Diameter distribution of the emerging bubbles close to the generator. The median of 23.1 mm is used for further processing.

3. Camera Set-up, Particle Image and Calibration

For the present measurements an off-the-shelf rotary-wing drone *DJI Mini 3 pro* with a take-off weight of 249 g, which is equipped with an $1/1.3''$ CMOS sensor was used. The sensor features an overall resolution of 8064 $\times$ 6048 px, where a 4k-resolution (3840 $\times$ 2160 px) was available within video mode at a repetition rate of max. 60 fps with a video bitrate of 150 Mbps. The pixel size is stated as 2.4 µm (DJI, 2024), using so-called *quad bayer coding*, where four pixels are combined. According to the manufacturer the lens is equipped with a 24 mm equivalent focal length with a fixed aperture of $f/1.7$. Since the camera set-up is fixed an easier calibration procedure can be conducted as explained later. The uncertainty in hover mode is stated as ± 0.1 m according to the data sheet of the manufacturer (DJI, 2024).

To extract the bubble diameter of the tracked glare points the relative angle between the illumination source, the camera and the bubble has to be known. The experimental test campaign took place on May, 8$^{\text{th}}$ 2024 at the inner courtyard of the ISM building at TU Braunschweig (52° 18′ 50.122" N, 10° 32′ 42.261" E). The evaluated video started at 16:22 (UTC+2) and had a recording time of 5 min. The solar elevation angle varies in this time period from $39.38°$ - $38.7°$, compared to the horizon (HOFFIsoft Software, 2024). The camera was turned down to $-90°$ for a parallelization of the focus layer and the ground. The focus was set to the ground and manual focus was activated, such that no undesired refocusing occurs during the measurement. With the solar elevation angle and the position of the camera the glare-point distance D_G could be calculated. Given θ is the angle between the camera and the illumination source, this value varies between $\theta = 50.62 - 51.3°$. If the mean value is taken, this yields an angle of $\theta = 50.96°$ and a corresponding value of $D_G = D_B \sin(\theta/2) \approx 0.43\ D_B$.

Figure 4a shows an inverted raw data image with several bubbles at different distances to the camera and so with a different magnification. For bubbles imaged with a higher magnification the outer edge is visible. All bubbles feature as unifying characteristic glare points as dominant detection attribute. The number however changes, due to light reflections from the glass walls nearby and the illumination angle. The focal layer was set close to infinity, consequently the bubbles closer to the lens experience some out-of-focus behavior, which is visible in the formation of polygonal glare points. Caused by the RGB sensor of the drone, different hue intensities becomes visible, which are a function of the (local) bubble-wall thickness γ. The glare-point distances in this example are located between $10 - 120$ px, which corresponds to a distance from the camera of $0.5 - 3.2$ m for the given experimental set-up. Further tests with larger distances up-to 8 m, showed a particle image with a glare-point distance of 5 px between the two respective maxima. Hence, for the presented magnification and camera set-up given by the *DJI Mini 3 pro*, the limit in height can be determined when the two most-dominant glare points collapse to one, which happened well above 10 m for the present set-up, which enables a theoretical investigation volume up-to 100 m^3.

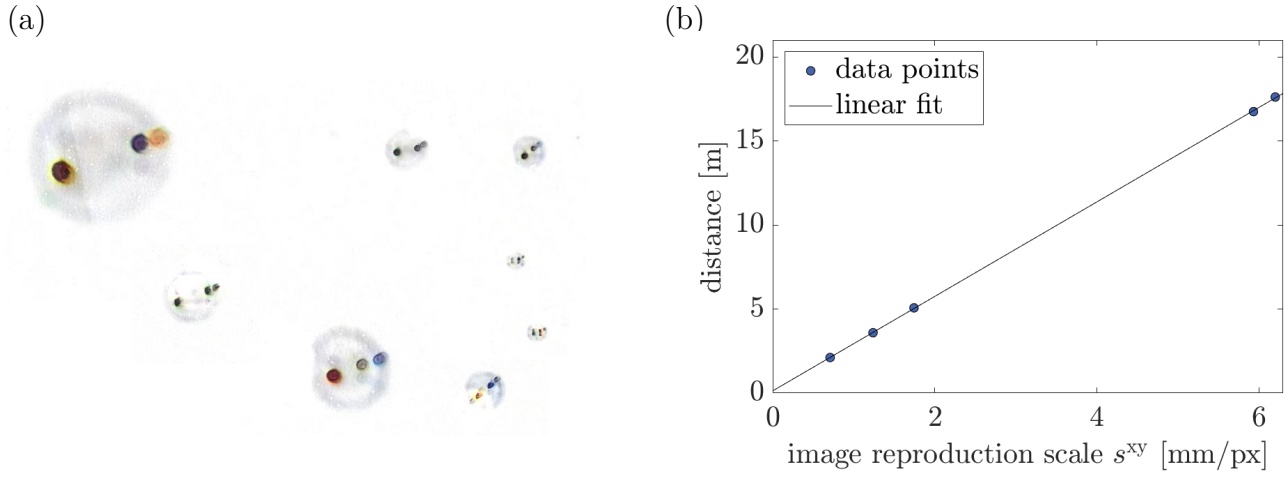

Figure 4. (a) Brightness-inverted raw-data image with background subtraction for several bubbles ranging from around 0.5 m up-to 3.2 m distance. (b) Diagram of the reproduction scale s^{xy} at different object-lens distances and the used interrelation for the glare-point approach.

The results of the calibration procedure are shown in Figure 4b. Caused by the fixed camera set-up within the drone, no extensive multi-point calibration procedure needed to be performed during the experiments, but this could be shifted to a controlled laboratory experiment in-advance, where all distances could be identified with higher precision. A laser-distance measurement device (*BOSCH Professional GLM 20*) was exerted to gain the distance from the lens to objects with a known vertical and/or horizontal extent parallel to the focus layer, which was set to infinity. It is important to mention, that no so-called *focus breathing* was recognized, such that, despite the actual focus layer position the gained reproduction scales are valid through-out all possible focus configurations. Figure 4b shows the fitted linear slope, that was used for the interrelation between

the glare-point distance and the distance in space from the bubble to the camera. After the calibration procedure, only a one-point calibration is necessary during the actual experiments, where a known geometrical pattern on the ground is used to validate the camera orientation parallel to the ground/horizon, to quantify the movement of the camera as shown in the next section and to double-check the glare-point distances with a known reproduction scale at a certain distance.

4. Moving Camera

As already mentioned the position uncertainty in hover mode of the camera drone is stated as ± 0.1 m in vertical direction and ± 0.3 m in horizontal direction. This value strongly depends on the local wind conditions and the availability of the positioning system e.g. the number of detected geo-positioning satellites. For each frame the camera states its horizontal and vertical position according to the geo-positioning coordinates and the internally built inertial measurement unit in a separate auxiliary file. These values are shown for the recorded time span in Figure 5 together with an image-based evaluation. The horizontal movement is tracked with a cross-correlation of each consecutive time step with 100 × 100 px image part, where no tracers are visible. The GPS-based analysis is much coarser, but also fulfills the stated uncertainty of around ± 0.1 m. The imaged-based displacement is an order-of-magnitude smaller, such that a different x-axis needs to be employed. As comparison a displacement of 0.05 m would result in a pixel displacement of 45 px for the current set-up. The actual pixel displacement reaches 1.5 px as maximum value. These small values of a frame-to-frame camera movement can be corrected easily during post-processing, such that the use of a moving camera isn't considered as drawback for the present undertaking.

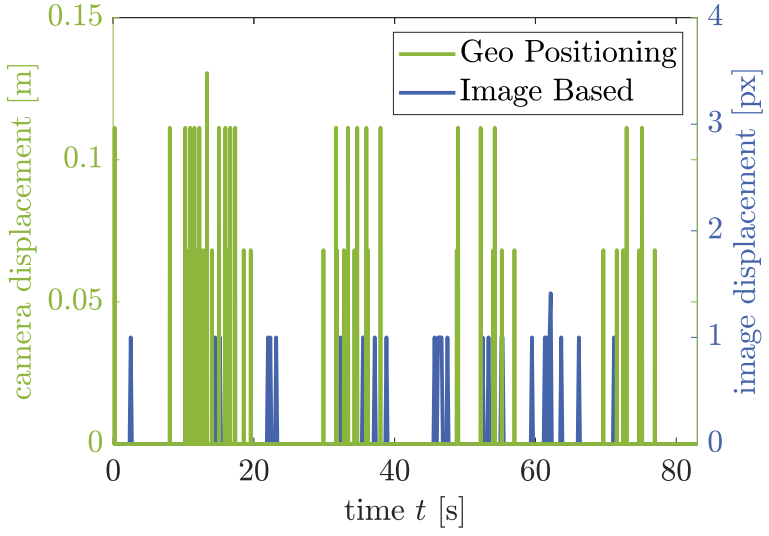

Figure 5. Frame-to-frame variability based on the sensors of the drone (•) and an image-based analysis (•) according to the recorded raw data.

5. Findings of the flow tracks

As exemplary show case the ground effects of the used drone are studied. The drone hovers in a height of around 3.2 m, the camera is directed parallel to the ground and bubbles are supplied from two bubble generators located outside the FOV. The FOV spans a ground area of 2.4 $\times$ 4.3 m^2, which gives a volume of 10.3 m^3, considering the pyramidal shape of the imaging volume. Many bubbles enter the FOV close to the ground conditioned by the generator positions. Some are experiencing an early lift and are entering the FOV from above and consequently experience the rotor down wash, which leads to a sudden acceleration and a relatively large vertical velocity, before experiencing the ground effects. Figure 6 shows exemplary-chosen bubbles to illustrate this downwards movement and the successfully tracking procedure. Figure 6a depicts the image coordinates for four bubbles in a time span of 1.47 s, which corresponds to 88 frames. Several bubbles in vicinity to the ground entered the FOV of the drone as well, which are visible in the lower part of the image. Figure 6b shows some tracks of bubbles experiencing a rotor down wash, where the acceleration is high close to the camera and consequently are certain amount of miss-positioning caused by an observed bubble deformation happens. This explored deformation diminishes after a few frames.

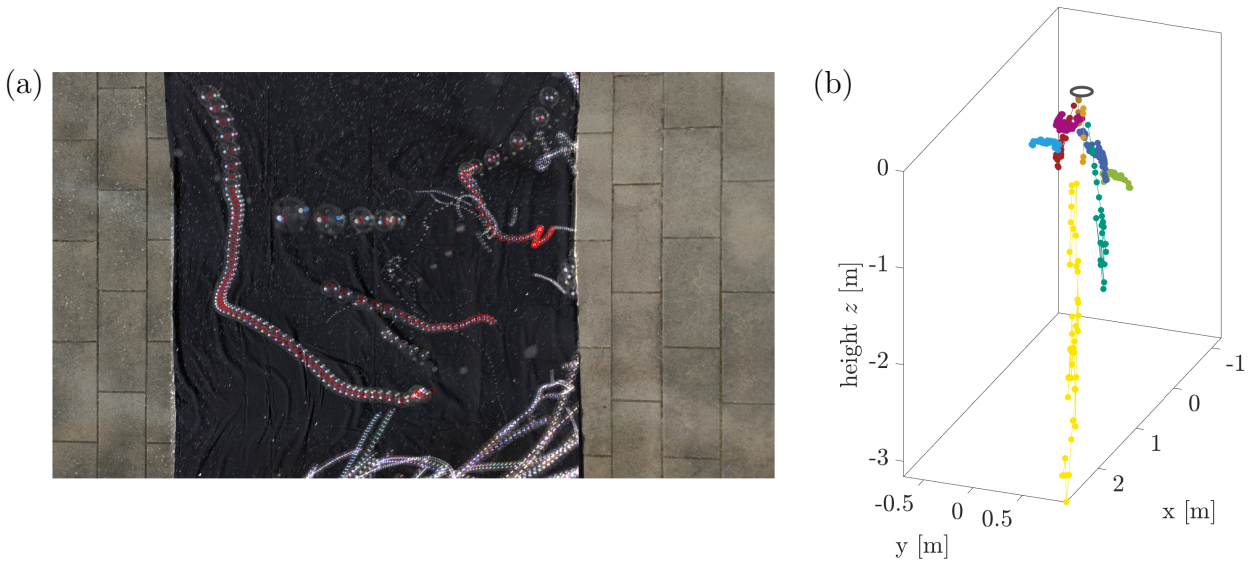

Figure 6. (a) Multi-exposed raw data image with four distinct bubbles and the corresponding tracks (○) in image coordinates. (b) Flow tracks in physical coordinates with applied calibration based on the glare-point tracking approach for bubbles experiencing a rotor down wash. The calculated drone position is indicated with a black circle.

6. Conclusions and Outlook

The present contribution provides an assessment of the suitability of drones used for large-scale particle tracking, where the integrated consumer-grade camera serves as imaging set-up. As tracer particles air-filled soap bubbles are used with a median diameter distribution in the order of $20 - 25$ mm. We made use of the sun as illumination source to track the glare points arise on the bubble as dominant detection attribute, which could be captured by the imaging sensor. The distances between the two most distinct glare points are used for a 3D3C reconstruction of the flow. Overall the use of a drone as imaging equipment proves successful for such an experiment. The slight permanent frame-by-frame movement of the drone in hover mode can be quantified by an image-based approach and corrected for each individual frame. The limits of the bubbles as tracers, are a limited following behavior, such that strong shear layers and intense accelerations need to be avoided. By a permanent tracking of the glare-point distance of each bubble an indication for bad following behavior could be identified. If larger volumes beyond 100 m^3 are of interest larger bubbles or a higher sensor resolution can be employed.
The concluding exemplary test case demonstrates an area of potential applications, where drones as imaging device could be of help to answer fluid-related questions. For large-scale facilities or difficult accessible terrain such a set-up can depict its strengths, since the image calibration can be done before-hand, due to the fixed camera set-up.

References

Detert, M., Cao, L., & Albayrak, I. (2019). Airborne image velocimetry measurements at the hydropower plant schiffmühle on limmat river, switzerland. In *Proceedings of the 2nd international symposium and exhibition on hydro-environment sensors and software, hydrosensoft 2019.* Retrieved from https://doi.org/10.3929/ethz-b-000341626

Detert, M., & Weitbrecht, V. (2014). Helicopter-based surface piv experiments at thur river. In *Proceedings of the seventh international conference on river flow, lausanne, switzerland.* Retrieved from https://doi.org/10.1201/b17133

Detert, M., & Weitbrecht, V. (2015). A low-cost airborne velocimetry system: proof of concept. *Journal of Hydraulic Research*, *53*(4), 532–539. Retrieved from https://doi.org/10.1080/00221686.2015.1054322

DJI. (2024). *Dji mini 3 pro.* Retrieved 2024-05-24, from https://www.dji.com/uk/mini-3-pro

Fuchs, T., Bross, M., & Kähler, C. J. (2023). Wall-shear-stress measurements using volumetric µptv. *Experiments in Fluids*, *64*(115). Retrieved from https://doi.org/10.1007/s00348-023-03656-1

Fujita, I., & Hino, T. (2003). Unseeded and seeded piv measurements of river flows videotaped from a helicopter. *Journal of Visualization*, *6*, 245-252. Retrieved from https://doi.org/10.1007/BF03181465

HOFFIsoft Software. (2024). *Online tool sun position.* Retrieved 2024-05-24, from https://www.sonnenverlauf.de/#/52.3139,10.5451,18/2024.05.08/16:27/1/1

Hou, J., Kaiser, F., Sciacchitano, A., & Rival, D. E. (2021). A novel single-camera approach to large-scale, three-dimensional particle tracking based on glare-point spacing. *Experiments in Fluids*, *62*(100), 1432-1114. Retrieved from https://doi.org/10.1007/s00348-021-03178-8

Kaiser, F., & Rival, D. E. (2023, aug). Large-scale volumetric particle tracking using a single camera: Analysis of the scalability and accuracy of glare-point particle tracking. *Experiments in Fluids*, *64*(149). Retrieved from https://doi.org/10.1007/s00348-023-03682-z

Raffel, M., Willert, C. E., Scarano, F., Kähler, C. J., Wereley, S., & Kompenhans, J. (2018). *Particle image velocimetry* (3rd ed.). Cham: Springer Berlin Heidelberg. doi: 10.1007/978-3-319-68852-7

Rosi, G. A., Sherry, M., Kinzel, M., & Rival, D. E. (2014). Characterizing the lower log region of the atmospheric surface layer via large-scale particle tracking velocimetry. *Experiments in Fluids*, *55*. Retrieved from https://doi.org/10.1007/s00348-014-1736-2

Wei, N. J., Brownstein, I. D., Cardona, J. L., Howland, M. F., & Dabiri, J. O. (2021). Near-wake structure of full-scale vertical-axis wind turbines. *Journal of Fluid Mechanics*, *914*, A17. Retrieved from https://doi.org/10.1017/jfm.2020.578